

## Identifiers

DOI 10.46298/jtcam.10170

HAL hal-03817307v4

## History

Received Oct 18, 2022

Accepted Jun 29, 2024

Published Feb 5, 2025

## Associate Editor

Olivier THOMAS

## Reviewers

Tao Fu

Anonymous

## Open Review

HAL hal-04819388

## Supplementary Material

Data

DOI 10.5281/zenodo.14764156

## Licence

CC BY 4.0

©The Authors

# On the bifurcation analysis of thin multilayer structures by the Asymptotic Numerical Method

Hamza AZZAYANI, Hamid ZAHROUNI, Norman MATHIEU, Pascal VENTURA, Michael BRUN, and Michel POTIER-FERRY

Université de Lorraine, CNRS, Arts et Métiers, LEM3, Metz, France

Laboratory of excellence on Design of Alloy Metals for low-mAss Structures (DAMAS), Université de Lorraine, France

This paper focuses on the stability analysis of multilayer thin shells using the asymptotic numerical method (ANM) combined with Padé approximants. This technique is highly effective for solving nonlinear problems due to its high-order algorithm that ensures accurate computation of singular points along nonlinear solution branches. We present various methods for detecting bifurcation points. The first technique uses a bifurcation indicator integrated into the nonlinear problem as a scalar function. This function represents the intensity of a fictitious perturbation force, evaluated along the equilibrium branch and vanishing exactly at singular points. The second method employs Padé approximants as a bifurcation indicator by analyzing the denominator of rational fractions. The third method identifies singular points by combining buckling and linear vibrations, examining the evolution of natural frequencies along the equilibrium path. The paper evaluates these three bifurcation detection techniques for multilayer composite structures. It also analyses the impact of the solution representation by power series or Padé approximants, the truncation order, and the accuracy parameter on the solution path.

**Keywords:** Asymptotic numerical method, instability, bifurcation, Padé approximants, thin multilayer structures

## 1 Introduction

Numerical modeling of structural problems has become an indispensable tool since the development of the finite element method, allowing a better understanding of the phenomena that occur during deformation. For reasons of cost and competitiveness, manufacturers tend to use light materials and complex structures such as auxetic mechanical metamaterials (Zhao and Fu 2023; Zhou et al. 2023; Wang et al. 2020; Zhao et al. 2023). Multilayer composite shell structures have been widely employed in civil engineering, aerospace, automotive, energy and many others (for example: thermal protection of satellite launch tanks (Toor 2018), printed circuit boards (Wang et al. 2006; Kim et al. 2015), morphing airfoils (Diaconu et al. 2008)). However, these structures are very sensitive to instabilities (e.g. buckling) (Ramm 2012; Kumar Yadav and Gerasimidis 2019), and are subjected to a drastic reduction of the critical load in the presence of geometrical or material defects. This instability often presents complex mechanical behaviors with large deformation, strong nonlinearity, multiple bifurcation points and multiple equilibrium paths. In the context of multilayer materials, the instability is very sensitive to the geometry, the number of layers in the thickness, their orientations and the anisotropic material properties (Brunetti et al. 2018; Finot and Suresh 1996). In order to have a better understanding of the complex instability phenomena in various materials, numerous experimental studies as well as analytical and numerical models have been developed (El Chebair et al. 1989; Frulloni et al. 2007; Fu et al. 2021). One application of these numerical models is the design of stacking sequences to obtain multi-stable structures, i.e. structures having several stable states for the same loads. The corresponding load-displacement curves are highly nonlinear with many bifurcations and stability changes, see (Kuang et al. 2021).

Nonlinear problems in structural mechanics are usually solved by iterative methods based on the predictor-corrector process. The principle is to follow the nonlinear solution branch of the

problem point by point in two steps. The first step is to linearize the initial nonlinear problem and predict a solution, and the second step is to correct the residual by successive iterations to reach the equilibrium. This method is widely used in finite element codes. However, the computation time remains a major obstacle of this method. For instability problems, these algorithms require an appropriate path-following strategy to follow complex response branches. A second approach to solve nonlinear problems is the perturbation technique. Here, the solution branch is established as a power series with respect to a parameter  $a$ , which can be defined similarly to the control parameters in classical iterative algorithms. This method is based on an analytical development and the applications were limited to particular problems with simple geometry.

The asymptotic numerical method (ANM) based on the perturbation technique presents an alternative (Damil and Potier-Ferry 1990). It solves nonlinear problems by combining asymptotic developments and numerical methods. The unknowns of the problem are developed in power series. ANM transforms the nonlinear problem into a succession of linear problems admitting the same tangent stiffness operator. Then, these problems are solved by a numerical method such as the finite element method (FEM). The ANM allows to compute a large part of the nonlinear branch with only one decomposition of the stiffness matrix per step (Cochelin 1994; Zahrouni et al. 1999). Many studies have been presented in the literature to compare the number of matrix decompositions required for a given solution path using the asymptotic numerical method or more classical approaches. The ANM has been the most efficient compared to the Newton-Raphson methods (Zahrouni et al. 1999). Since power series have a limited convergence radius, a continuation technique has been proposed to obtain the whole solution branch. Each end of step will serve as the starting point of the next step and the step length is computed a posteriori, requiring that the relative difference between solutions at two consecutive orders is less than a user-defined accuracy parameter. The automatic determination of the step lengths based on series terms and according to the local nonlinearity of the response curve is the key point for the efficiency and robustness of these methods compared to classical iterative methods. ANM has been successfully applied in many fields: plastic beams (Abichou et al. 2002; Assidi et al. 2009), Navier-Stokes equation (Cadou et al. 2001), contact mechanics (Elhage-Hussein et al. 2000), instability of fiber reinforced composites (Xu et al. 2019) and many others.

The use of a rational representation (Padé approximants (Baker and Graves-Morris 1981)) instead of a polynomial representation improves the validity range of the solution (Elhage-Hussein et al. 2000). Najah et al. (Najah et al. 1998) have shown the efficiency of the Padé approximants over the power series representation and the Rayleigh-Ritz technique (Najah et al. 1998; Noor and Peters 1980). Using rational fractions with a common denominator can help minimize the number of poles. This can be particularly useful in the context of numerical methods, where a large number of poles can lead to computational inefficiencies.

Within ANM framework, bifurcation indicators have been proposed to identify critical points. A first indicator is a scalar function computed by introducing a fictitious perturbation force in the equilibrium problem (Boutyour et al. 2004). The indicator can be determined explicitly along the equilibrium branch by the perturbation technique. The roots of this function characterize the singular points (Tri et al. 2014). The second indicator consists in analyzing the poles of the rational representation. Overall, the bifurcation point corresponds to the smallest real pole of the Padé approximant (Boutyour et al. 2004). A third technique for identifying singular points combines buckling and vibration analysis. The method starts with the calculation of the equilibrium branch. Then, we proceed to the determination of the eigenfrequencies with the corresponding vibration modes around this branch. In this method, natural frequencies are used as bifurcation indicator. Several studies show that the natural frequencies decrease when the applied load increases and their roots correspond to critical points (bifurcation points or limit points) (Boutyour et al. 2006).

This paper examines the application of three previously discussed bifurcation detection methods to multilayer composite shells. The aim is to assess the reliability of these techniques in the context of strong geometrical nonlinearities. The results are not limited to the first bifurcation point, which is the most critical, but allow the detection of all possible bifurcation points of a shell structure, which constitutes an improvement regarding the state of the art. We also analyze the influence of solution representation (polynomial or rational), truncation order, and accuracy

parameter on the equilibrium path.

In what follows, Section 2 presents the shell formulation and the asymptotic numerical algorithm for solving the resulting nonlinear problem. Section 3 gives details about the three techniques used to detect bifurcation points. Section 4 presents some numerical results and Section 5 concludes our study.

## 2 Static shell formulation and resolution algorithm

### 2.1 Geometric and kinematic description

In this paper, we consider perfectly bonded multilayer thin structures. The behavior of each layer is orthotropic elastic. While this limits the practical applications to small deformations, it does allow large rotations to occur. A shell formulation, adapted for large displacements and rotations, using only displacement variables is used (Büchter et al. 1994). Figure 1 shows the geometry and kinematics of the proposed shell in the reference and deformed configuration. The position

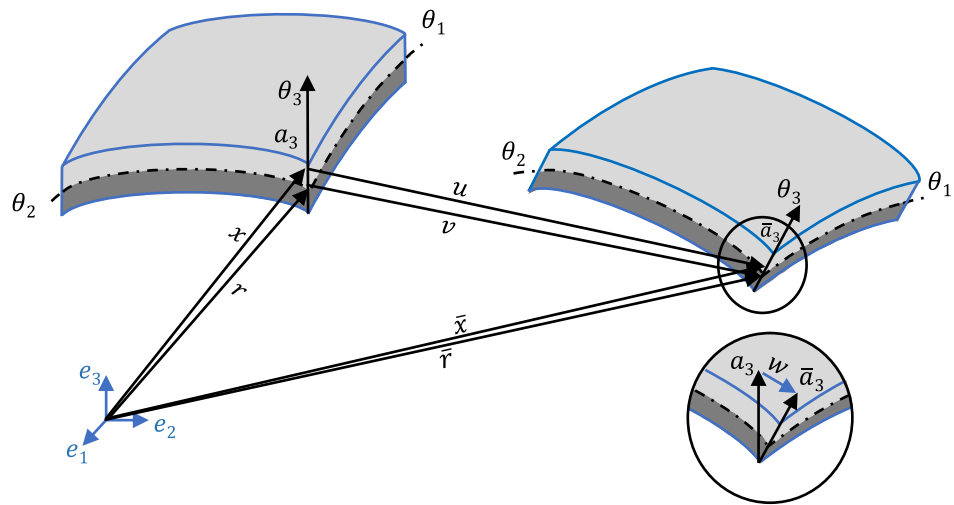


**Figure 1** Geometric and kinematic description of the shell.

vector of an arbitrary material point in the initial configuration is

$$\mathbf{x}(\theta_1, \theta_2, \theta_3) = \mathbf{r}(\theta_1, \theta_2) + \theta_3 \mathbf{a}_3(\theta_1, \theta_2) \quad (1)$$

where  $\mathbf{r}$  is the projection of this point on the mid-surface,  $\mathbf{a}_3$  the shell director vector and  $(\theta_1, \theta_2, \theta_3)$  the curvilinear coordinates. Then, the covariant basis vectors in the undeformed configuration  $\mathbf{g}_i$  are expressed as

$$\begin{aligned} \mathbf{g}_\alpha &= \frac{\partial \mathbf{x}}{\partial \theta_\alpha} = \mathbf{r}_{,\alpha} + \theta_3 \mathbf{a}_{3,\alpha}, \quad \alpha = 1, 2 \\ \mathbf{g}_3 &= \frac{\partial \mathbf{x}}{\partial \theta_3} = \mathbf{a}_3 \end{aligned} \quad (2)$$

where  $_{,\alpha} = \frac{\partial}{\partial \theta_\alpha}$ .

Assuming a linear variation of the displacement in the thickness direction, the displacement field corresponding to the deformed configuration can be written as

$$\mathbf{u}(\theta_1, \theta_2, \theta_3) = \mathbf{v}(\theta_1, \theta_2) + \theta_3 \mathbf{w}(\theta_1, \theta_2) \quad (3)$$

where  $\mathbf{v}$  and  $\mathbf{w}$  represent, respectively, the mid-surface displacement and the difference vector between the undeformed and deformed shell director vectors. In this formulation, six degrees of freedom can be distinguished,  $(v_1, v_2, v_3)$  are relative to the translation of the mid-surface and  $(w_1, w_2, w_3)$  updating the director vector. Thus, the position vector of the deformed shell can be defined as

$$\bar{\mathbf{x}} = (\mathbf{r} + \mathbf{v}) + \theta_3 (\mathbf{a}_3 + \mathbf{w}) = \bar{\mathbf{r}} + \theta_3 \bar{\mathbf{a}}_3. \quad (4)$$

Similar to Equation (2), the covariant basis vectors in the deformed configuration  $\bar{\mathbf{g}}_i$  are

$$\begin{aligned}\bar{\mathbf{g}}_\alpha &= \frac{\partial \bar{\mathbf{x}}}{\partial \theta_\alpha} = \bar{\mathbf{r}}_{,\alpha} + \theta_3 \bar{\mathbf{a}}_{3,\alpha}, \quad \alpha = 1, 2 \\ \bar{\mathbf{g}}_3 &= \frac{\partial \bar{\mathbf{x}}}{\partial \theta_3} = \bar{\mathbf{a}}_3.\end{aligned}\quad (5)$$

For more details on this formulation, please refer to the work by Büchter et al. (1994).

## 2.2 Strain and stress equations

The Green-Lagrange strain tensor is written in the contravariant basis:

$$\boldsymbol{\gamma} = \frac{1}{2}(\bar{\mathbf{g}}_{ij} - \mathbf{g}_{ij})\mathbf{g}^i \otimes \mathbf{g}^j \quad \text{with} \quad \mathbf{g}_{ij} = \mathbf{g}_i \cdot \mathbf{g}_j \quad (6)$$

where  $\mathbf{g}_{ij}$  and  $\bar{\mathbf{g}}_{ij}$  are the covariant components of the metric tensors in the reference and deformed configurations, respectively, and  $\mathbf{g}^i$  denotes the contravariant basis vectors. The contravariant basis vectors can be defined by the orthogonality condition  $\mathbf{g}^i \cdot \mathbf{g}_j = \delta_j^i$ .

From Equations (2) and (5), the components of the Green-Lagrange strain can be written as

$$\gamma_{ij} = \alpha_{ij} + \beta_{ij}\theta_3 + Q_{ij}(\theta_3)^2 \quad (7)$$

with  $\alpha_{ij} = \frac{1}{2}(\bar{\mathbf{a}}_i \bar{\mathbf{a}}_j - \mathbf{a}_i \mathbf{a}_j)$ ,  $\beta_{\alpha\beta} = \frac{1}{2}(\bar{\mathbf{a}}_{3,\alpha} \bar{\mathbf{a}}_\beta + \bar{\mathbf{a}}_{3,\beta} \bar{\mathbf{a}}_\alpha - \mathbf{a}_{3,\alpha} \mathbf{a}_\beta - \mathbf{a}_{3,\beta} \mathbf{a}_\alpha)$ ,  $\beta_{\alpha 3} = \frac{1}{2}(\bar{\mathbf{a}}_{3,\alpha} \bar{\mathbf{a}}_3 - \mathbf{a}_{3,\alpha} \mathbf{a}_3)$ ,  $Q_{\alpha\beta} = \frac{1}{2}(\bar{\mathbf{a}}_{3,\alpha} \bar{\mathbf{a}}_{3,\beta} - \mathbf{a}_{3,\alpha} \mathbf{a}_{3,\beta})$ , and  $\beta_{33} = Q_{\alpha 3} = Q_{33} = 0$ .

To avoid numerical locking in shell modeling, the EAS (Enhanced Assumed Strain) concept proposed by Simo and Rifai (1990) will be used. This method consists in introducing an additional strain field  $\tilde{\boldsymbol{\gamma}}$  incompatible with the displacement and which is chosen, by construction, orthogonal to the stress field  $S^m$  of each layer  $m$ . Let us underline that the orthogonality condition has no physical meaning. This is only a manner to establish a consistent transition  $3D \rightarrow 2D$  or  $3D \rightarrow$  shell. This additional variable allows to use a complete 3D constitutive law without condensation. Since no inter-element continuity is required, the additional deformation is eliminated at the elementary level, thus preserving the formal structure of a 6-parameter shell theory. The incompatible strain field  $\tilde{\boldsymbol{\gamma}}$  reads

$$\tilde{\boldsymbol{\gamma}} = \theta_3 \tilde{\beta}_{33} \mathbf{g}^3 \otimes \mathbf{g}^3 \quad (8)$$

and the orthogonality condition is

$$\int_{\Omega} ({}^t S^m : \tilde{\boldsymbol{\gamma}}) d\Omega = 0. \quad (9)$$

The term  $\tilde{\beta}_{33}$  provides a linear variation of the strain field through the thickness. Thus, the total strain field  $\boldsymbol{\gamma}$  and the stress field (second Piola-Kirchhoff stress tensor) in each layer  $S^m$  read

$$\boldsymbol{\gamma} = \boldsymbol{\gamma}_u + \tilde{\boldsymbol{\gamma}} = (\boldsymbol{\gamma}_l(\mathbf{u}) + \boldsymbol{\gamma}_{nl}(\mathbf{u}, \mathbf{u})) + \tilde{\boldsymbol{\gamma}} \quad (10)$$

$$S^m = D^m : \boldsymbol{\gamma} \quad (11)$$

in which  $\boldsymbol{\gamma}_l(\mathbf{u})$  and  $\boldsymbol{\gamma}_{nl}(\mathbf{u}, \mathbf{u})$  denote the linear and nonlinear parts of the compatible strain field, respectively, and  $D^m = D^{ijkl(m)} \mathbf{g}_i \otimes \mathbf{g}_j \otimes \mathbf{g}_k \otimes \mathbf{g}_l$  refers to the fourth-order elasticity tensor of the  $m$ th layer. As the elasticity tensor is often obtained in Cartesian coordinates, a transformation to curvilinear coordinates is used in the numerical implementation and formulated as

$$D^{ijkl(m)} = C^{pqrs(m)} (\mathbf{e}_p \cdot \mathbf{g}^i) (\mathbf{e}_q \cdot \mathbf{g}^j) (\mathbf{e}_r \cdot \mathbf{g}^k) (\mathbf{e}_s \cdot \mathbf{g}^l) \quad (12)$$

where  $C^{pqrs(m)}$  presents the components of elasticity tensor in Cartesian coordinates.

### 2.3 A three-field variational formulation

Let us consider a material domain  $\Omega$  which will consist in a shell structure. The shell formulation considered in the present study is based on a three-dimensional formulation. The unknowns are the displacement field  $\mathbf{u}$ , the Green-Lagrange strain  $\boldsymbol{\gamma}$  and the second Piola-Kirchhoff stress tensor in the  $m$ th layer  $S^m$ . A consistent functional framework can be obtained by considering Sobolev spaces:  $u_i \in W^{1,4}(\Omega)$ ,  $\tilde{\gamma}_{ij} \in L^2(\Omega)$  and  $S_{ij}^m \in L^2(\Omega)$ . The equations of the problem are equivalent to the stationarity of the Hu-Washizu functional, which is written

$$\pi_{\text{HW}}(\mathbf{u}, \boldsymbol{\gamma}, S^m) = \sum_{m=1}^N \int_{\Omega} \left\{ \frac{1}{2} {}^t \boldsymbol{\gamma} : D^m : \boldsymbol{\gamma} - {}^t S^m : (\boldsymbol{\gamma} - \boldsymbol{\gamma}_u) \right\} d\Omega - \lambda P_e(\mathbf{u}) \quad (13)$$

where  $N$  refers to the number of layers of laminated shells and  $\lambda P_e(\mathbf{u})$  is the work of the external forces ( $\lambda$  is a scalar load parameter). Considering the orthogonality condition (9) between the stress field in the  $m$ th layer  $S^m$  and the additional strain field  $\tilde{\boldsymbol{\gamma}}$ , Equation (13) becomes

$$\pi_{\text{EAS}}(\mathbf{u}, \tilde{\boldsymbol{\gamma}}) = \sum_{m=1}^N \int_{\Omega} \frac{1}{2} {}^t (\boldsymbol{\gamma}_u + \tilde{\boldsymbol{\gamma}}) : D^m : (\boldsymbol{\gamma}_u + \tilde{\boldsymbol{\gamma}}) d\Omega - \lambda P_e(\mathbf{u}). \quad (14)$$

Thus, the variational problem is

$$\delta \pi_{\text{EAS}}(\mathbf{u}, \tilde{\boldsymbol{\gamma}}) = \sum_{m=1}^N \int_{\Omega} {}^t (\delta \boldsymbol{\gamma}_u + \delta \tilde{\boldsymbol{\gamma}}) : D^m : (\boldsymbol{\gamma}_u + \tilde{\boldsymbol{\gamma}}) d\Omega - \lambda P_e(\delta \mathbf{u}). \quad (15)$$

This formulation is not the optimal one for applying the perturbation technique because the equilibrium equation is cubic with respect to the displacement field  $\mathbf{u}$ . High efficiency can be achieved by employing a variational formulation within a quadratic framework, which is easily accomplished by reintroducing the stress field and the constitutive law, as detailed in (Azrar et al. 1993). Thus, the variational problem leads to the equilibrium equation, the compatibility equation which is equivalent to the orthogonality condition and the constitutive equation

$$\sum_{m=1}^N \int_{\Omega} \delta \boldsymbol{\gamma}_u : S^m d\Omega - \lambda P_e(\delta \mathbf{u}) = 0 \quad (16)$$

$$\sum_{m=1}^N \int_{\Omega} \delta \tilde{\boldsymbol{\gamma}} : S^m d\Omega = 0 \quad (17)$$

with  $S^m = D^m : (\boldsymbol{\gamma}_u + \tilde{\boldsymbol{\gamma}})$ . Equations (16) and (17) are quadratic with respect to the unknowns and can be expressed in the general form (Cochelin et al. 2007)

$$\mathbf{R}(\mathbf{U}, \lambda) = \mathbf{L}(\mathbf{U}) + \mathbf{Q}(\mathbf{U}, \mathbf{U}) - \lambda \mathbf{F} = \mathbf{0} \quad (18)$$

where  $\mathbf{U} = (\mathbf{u}, \tilde{\boldsymbol{\gamma}}, S^m)$  is a unknown vector,  $\mathbf{L}(\cdot)$  a linear operator,  $\mathbf{Q}(\cdot, \cdot)$  a quadratic one,  $\mathbf{F}$  the external load vector and  $\mathbf{R}$  the residual vector. Thus, the problem is to find the mixed variable  $\mathbf{U}$  and the loading parameter  $\lambda$  verifying Equation (18).

### 2.4 Asymptotic numerical algorithm

We propose to solve Equation (18) by the Asymptotic Numerical Method (Büchter et al. 1994). First, we use the perturbation technique to transform the nonlinear problem into a succession of linear ones all admitting the same tangent operator. The resulting problems up to order  $p$  are discretized and solved by the finite element method. Thus, we analytically obtain a part of the solution path with only one stiffness matrix decomposition. Compared to the predictor-corrector method such as Riks method, this approach is automatic and more efficient (Najah et al. 1998).

Starting from an initially known solution  $(\mathbf{U}_0, \lambda_0)$ , the perturbation technique consists in searching the solution path of the nonlinear problem under an asymptotic expansion form with respect to a path parameter  $a$ :

$$\begin{aligned} \mathbf{U}(a) &= \mathbf{U}_0 + a\mathbf{U}_1 + a^2\mathbf{U}_2 + \dots + a^n\mathbf{U}_n \\ \lambda(a) &= \lambda_0 + a\lambda_1 + a^2\lambda_2 + \dots + a^n\lambda_n \end{aligned} \quad (19)$$

in which  $U_p$  are mixed unknown vectors,  $\lambda_p$  the unknown coefficients at order  $p$ , and  $n$  is the truncation order of the series. By analogy with arc-length iterative methods, the control parameter  $a$  is chosen as the projection of the displacement increment  $(\mathbf{u} - \mathbf{u}_0)$  and the load increment  $(\lambda - \lambda_0)$  on the tangent direction  $(\mathbf{u}_1, \lambda_1)$ , where  $\langle \cdot, \cdot \rangle$  is the Euclidean scalar product

$$a = \langle \mathbf{u} - \mathbf{u}_0, \mathbf{u}_1 \rangle + (\lambda - \lambda_0)\lambda_1. \quad (20)$$

By substituting Equation (19) into Equations (18) and (20) and identifying the terms according to the power of  $a$ , we obtain a recurrent sequence of linear mixed problems admitting the same tangent operator.

- Order 1:

$$\begin{aligned} L_t^0(U_1) &= \lambda_1 F \\ \langle \mathbf{u}_1, \mathbf{u}_1 \rangle + \lambda_1^2 &= 1 \end{aligned} \quad (21)$$

- Order 2:

$$\begin{aligned} L_t^0(U_2) &= \lambda_2 F - Q(U_1, U_1) \\ \langle \mathbf{u}_2, \mathbf{u}_1 \rangle + \lambda_2 \lambda_1 &= 0 \end{aligned} \quad (22)$$

- Order  $p$ :

$$\begin{aligned} L_t^0(U_p) &= \lambda_p F - \sum_{r=1}^{p-1} Q(U_r, U_{p-r}) \\ \langle \mathbf{u}_p, \mathbf{u}_1 \rangle + \lambda_p \lambda_1 &= 0 \end{aligned} \quad (23)$$

The tangent operator  $L_t^0$  depends only on the initial solution and is defined by:

$$L_t^0(\cdot) = L(\cdot) + Q(U_0, \cdot) + Q(\cdot, U_0) \quad (24)$$

The linear problems above are solved using the finite element method. For discretization, we use the eight node shell element with reduced integration as described in (Zahrouni et al. 1999). The finite element discretisation is described in Appendix A. The discretized form of the problem at order  $p$  ( $p \geq 2$ ) is given by

$$\begin{aligned} [K_t^0] \{ \mathbf{q}_p \} &= \lambda_p \{ F \} + \{ F_p^{\text{nl}} \} \\ {}^t \{ \mathbf{q}_p \} \{ \mathbf{q}_1 \} + \lambda_p \lambda_1 &= 0 \end{aligned} \quad (25)$$

where  $[K_t^0]$  is the classical tangent stiffness matrix at the starting point  $(U_0, \lambda_0)$ ,  $\{ F \}$  is the external force vector,  $\{ \mathbf{q}_p \}$  and  $\lambda_p$  are respectively the discretized form of the displacement  $\mathbf{u}_p$  and the loading parameter at order  $p$ . The second member  $\{ F_p^{\text{nl}} \}$  depends on the solutions computed at the previous  $(p - 1)$  orders.

In the ANM, the variables are expressed as power series expansions. These series have a validity range that depends on the problem to be solved, the truncated orders of the series, and the required accuracy. A simple continuation procedure consists of considering that the relative difference between the displacement series at two successive orders must remain small with respect to a critical value  $\delta_1$  (Cochelin 1994). Thus, the maximal value of the path parameter is

$$a_{\max} = \left( \delta_1 \frac{\| \mathbf{u}_1 \|}{\| \mathbf{u}_n \|} \right)^{\frac{1}{n-1}} \quad (26)$$

with  $\delta_1$  a user-defined accuracy parameter and  $\| \cdot \|$ , the Euclidean norm of the vector. The solution branch is obtained step by step by considering each end of step as the starting point of the next step. One of the originalities of this procedure is that the step length is determined a posteriori according to the characteristics of the computed series. This criterion avoids the user intervention to define the step length (which is often the case in commercial finite element software). Thus, this continuation algorithm is automatic, more robust and easier to use for predicting complex shell behaviors. We would also like to mention that the step length is automatically adaptive to the nonlinearity of the problem.

## 2.5 Convergence improvement by Padé approximants

In the previous section, we presented a continuation method based on the polynomial representation. The solution path is represented by truncated power series. Several tests have shown the efficiency and reliability of this algorithm (thin shells in Lagrangian formulation (Cochelin 1994; Cochelin et al. 1994), viscous fluid mechanics and plastic structures (Zahrouni et al. 1999)). In addition, the use of the rational representation, called Padé approximants, instead of the polynomial representation allows to increase the range of validity of the solution. For a more detailed study on Padé approximants, we refer the reader to (Baker and Graves-Morris 1981).

We denote  $P_n$  the representation by rational fractions of the displacement  $\mathbf{u}$  and the loading parameter  $\lambda$  for a truncation order  $n$ :

$$\begin{aligned} P_n(\mathbf{u}(a)) &= \mathbf{u}_0 + a \frac{D_{n-2}}{D_{n-1}} \mathbf{u}_1 + a^2 \frac{D_{n-3}}{D_{n-1}} \mathbf{u}_2 + \dots + a^{n-1} \frac{1}{D_{n-1}} \mathbf{u}_{n-1} \\ P_n(\lambda(a)) &= \lambda_0 + a \frac{D_{n-2}}{D_{n-1}} \lambda_1 + a^2 \frac{D_{n-3}}{D_{n-1}} \lambda_2 + \dots + a^{n-1} \frac{1}{D_{n-1}} \lambda_{n-1} \end{aligned} \quad (27)$$

where  $D_i(a) = 1 + ad_1 + a^2d_2 + \dots + a^i d_i$  are polynomials of degree  $i$  with real coefficients  $d_i$ , see (Elhage-Hussein et al. 2000).

These rational approximants have a common denominator to limit the number of poles of the representation. Using the same criterion of the polynomial representation based on displacement, we can define a range of validity ( $a_{\max_p}$ ) of the rational representation (27). In this case, we must require that the difference between two rational solutions at consecutive orders remains small at the end of the step. This can be expressed by

$$\frac{\|P_n(\mathbf{u}(a_{\max_p})) - P_{n-1}(\mathbf{u}(a_{\max_p}))\|}{\|P_n(\mathbf{u}(a_{\max_p})) - P_0\|} = \delta_2. \quad (28)$$

where  $\delta_2$  is a new accuracy parameter.

The range of validity  $a_{\max_p}$  is searched in the interval  $[a_{\max}; \beta a_{\max}]$  by the bisection method using the criterion in Equation (28), where  $\beta > 1$  is a user-defined parameter. The Padé approximants are computed by a simple Gram-Schmidt orthogonalization, which does not require too much computational time compared to the representation by series. Various examples have shown the efficiency and robustness of the Padé algorithm (Elhage-Hussein et al. 2000).

## 3 Bifurcation detection methods

### 3.1 Bifurcation indicator

The goal of this section is to develop a reliable algorithm, based on ANM, for the determination of bifurcation points. These points are detected by evaluating, along the equilibrium branch, a scalar function called bifurcation indicator. This scalar is obtained by introducing a fictitious perturbation force in the equilibrium problem, and which vanishes at the singular points. Several examples are presented to evaluate the efficiency of the proposed method (Boutyour et al. 2004).

Let  $\Delta\mu\mathbf{f}$  be a fictitious perturbation force applied to the structure in a deformed state  $(\mathbf{U}, \lambda)$ .  $\Delta\mu$  represents the intensity of the force and  $\Delta\mathbf{U} = (\Delta\mathbf{u}, \Delta\tilde{\mathbf{y}}, \Delta\mathbf{S}^m)$  its associated response. Under these conditions, the perturbed equilibrium equation is

$$L(\mathbf{U} + \Delta\mathbf{U}) + Q(\mathbf{U} + \Delta\mathbf{U}, \mathbf{U} + \Delta\mathbf{U}) = \lambda\mathbf{F} + \Delta\mu\mathbf{f}. \quad (29)$$

Considering the equilibrium equation (18) and neglecting the quadratic terms, the perturbed problem is written:

$$L_t(\Delta\mathbf{U}) = \Delta\mu\mathbf{f} \quad (30)$$

where  $L_t(\cdot) = L(\cdot) + Q(\mathbf{U}, \cdot) + Q(\cdot, \mathbf{U})$  is the tangent operator taken at the equilibrium point  $(\mathbf{U}, \lambda)$ . An additional condition based on the displacement is prescribed:

$$\langle L_t^0(\Delta\mathbf{U}) - \Delta\mathbf{U}_0, \Delta\mathbf{U}_0 \rangle = 0 \quad (31)$$

where  $L_t^0$  is the tangent operator at the starting point  $(U_0, \lambda_0)$ .

Equations (30) and (31) will be solved by the asymptotic numerical method and the unknowns  $\Delta U$  and  $\Delta \mu$  are written as power series:

$$\begin{aligned}\Delta U(a) &= \Delta U_0 + a\Delta U_1 + a^2\Delta U_2 + \dots + a^n\Delta U_n \\ \Delta \mu(a) &= \Delta \mu_0 + a\Delta \mu_1 + a^2\Delta \mu_2 + \dots + a^n\Delta \mu_n\end{aligned}\quad (32)$$

In the same way as the fundamental branch and by substituting Equation (32) in Equations (30) and (31), we obtain a sequence of linear problems.

- Order 0:

$$L_t^0(\Delta U_0) = \Delta \mu_0 f \quad (33)$$

$\Delta U_0$  is computed by imposing  $\Delta \mu_0 = 1$ .

- Order  $p \geq 1$ :

$$\begin{aligned}L_t^0(\Delta U_p) &= \Delta \mu_p f - \sum_{r=1}^p (Q(U_r, \Delta U_{p-r}) + Q(\Delta U_{p-r}, U_r)) \\ \langle \Delta U_p, f \rangle &= 0.\end{aligned}\quad (34)$$

The vectors  $U_r$  correspond exactly to those determined during the computation of the equilibrium branch. The application of the ANM requires the computation of a second series at each step. Nevertheless, the corresponding computation time remains less important, because the stiffness matrix used for the calculation of the equilibrium branch is the same for the bifurcation indicator.

Such as the equilibrium branch, the expansion terms of the series are determined by the finite element method after a condensation step. The discretization of the problem at order  $p$  leads to

$$\begin{aligned}[K_t^0]\{\Delta q_p\} &= \Delta \mu_p \{f\} + \{\Delta F_p^{nl}\} \\ {}^t\{\Delta q_p\}[K_t]\{\Delta q_0\} &= 0\end{aligned}\quad (35)$$

where  $[K_t^0]$  denotes the tangent stiffness matrix at the starting point,  $\{\Delta q_0\}$  and  $\{\Delta q_p\}$  are respectively the nodal displacement vectors at orders 0 and  $p$  associated to the perturbation force  $\{f\}$ . The vector  $\{\Delta F_p^{nl}\}$  depends on the solutions  $U$  up to order  $p$  and  $\Delta U$  up to order  $(p - 1)$ . Thus, Equation (35) yields

$$\Delta \mu_p = -\frac{\langle \Delta F_p^{nl}, \Delta q_0 \rangle}{\langle f, \Delta q_0 \rangle}. \quad (36)$$

From the terms  $\Delta \mu_p$  ( $1 \leq p \leq n$ ), we can construct the series development of  $\Delta \mu$  and study its sign along the equilibrium branch in order to detect the bifurcation.

### 3.2 Poles of the Padé approximants

Another simple method to detect bifurcation points is the analysis of the poles of the Padé approximants. The bifurcation points correspond to the real roots of the rational fraction denominator (Bouty et al. 2004; Tri et al. 2014). We note here another interest of the rational representation with respect to the polynomial representation.

### 3.3 Natural frequency of vibration

Buckling and vibration are instability phenomena that can coexist and induce large displacements generally causing damage in structural mechanics. The knowledge of the natural frequencies and the critical load with their corresponding mode shapes allows to predict the resonance and instability regions. A classical technique to combine vibration and buckling analysis is to start first with the computation of the equilibrium branch. The frequencies with the corresponding vibration modes around this branch are then determined. Several studies show that the natural frequencies decrease as the applied load increases and exactly cancel at the critical points (bifurcation points or limit points) (Bouty et al. 2006). We use the asymptotic numerical method to solve equilibrium and linear vibration problems. The unknowns of the problem



(solution branch, frequency and eigenmode) are determined by a perturbation technique whose terms are calculated by the finite element method.

For a given applied load, the structure is assumed to oscillate around a static state  $U$ . These oscillations are described by the time-dependent mixed vector  $V(\theta_1, \theta_2, \theta_3, t)$ , so the global response is written  $U(\theta_1, \theta_2, \theta_3) + V(\theta_1, \theta_2, \theta_3, t)$ . The oscillations of the structure around a static equilibrium state are described by

$$M(\ddot{V}) + L(U + V) + Q(U + V, U + V) = \lambda F \quad (37)$$

with

$$\langle M\ddot{V}, \delta U \rangle = \int_{\Omega} \rho(\ddot{v}_1 \delta u_1 + \ddot{v}_2 \delta u_2 + \ddot{v}_3 \delta u_3) d\Omega \quad (38)$$

where  $\ddot{V}$  is the second derivative with respect to time of  $V$  and the  $v_i$  are the components of the displacement  $V$ ,  $M$  is the mass matrix and  $\rho$  is the density. Neglecting the quadratic term in  $V$  through  $Q(V, V)$ , Equation (37) becomes

$$L_t(V) + M(\ddot{V}) = 0 \quad (39)$$

where  $L_t = L(\cdot) + Q(U, \cdot) + Q(\cdot, U)$  is the tangent operator at a static deformed state  $U$ . The general solution to Equation (39) is expressed as  $V = X e^{i\omega t}$ , and upon insertion into Equation (39) yields the linear eigenvalue problem

$$L_t(X) - \omega^2 M(X) = 0. \quad (40)$$

To study the eigenfrequencies  $\omega$  and their associated modes  $X$  in pre-buckling and post-buckling ranges, we need to solve the following coupled problem

$$L(U) + Q(U, U) = \lambda F \quad (41)$$

$$L_t(X) = \omega^2 M(X). \quad (42)$$

Equation (41) corresponds to the static displacement load solution. The obtained displacement  $U$  is used to compute the tangent operator  $L_t$ . Note that, if the static equilibrium  $U(\lambda)$  is stable, all the eigenvalues of Equation (42) are positive and  $\omega$  represents the natural frequencies. On the other hand, if  $U(\lambda)$  is unstable, Equation (42) has negative eigenvalues. The critical points correspond to the load value for which  $\omega = 0$ . This criterion will be used to detect the bifurcation points.

The static problem (41) has been solved using the ANM in Section 2.4. The same technique will be used to solve the dynamic problem (42). The idea is to determine analytically in power series form the unknowns  $(X, \omega)$

$$\begin{aligned} X &= X_0 + aX_1 + a^2X_2 + \dots + a^nX_n \\ \omega^2 &= \omega_0^2 + a\omega_1 + a^2\omega_2 + \dots + a^n\omega_n \end{aligned} \quad (43)$$

where  $(X_0, \omega_0^2)$  is the solution of the eigenvalue problem at the starting equilibrium point  $(U_0, \lambda_0)$ ,  $X_r = (u_{xr}, \tilde{y}_{xr}, s_{xr})$  is a mixed vector, and  $\omega_r$  is a scalar parameter. The parameter  $a$  is the same as in Equation (32). Substituting Equation (43) into Equation (42) and identifying the terms according to the power of  $a$ , we obtain a sequence of linear problems.

- Order 1:

$$L_t^0(X_1) - \omega_0^2 M X_1 = \omega_1 M X_0 - Q(U_1, X_0) - Q(X_0, U_1) \quad (44)$$

- Order  $r$ :

$$L_t^0(X_r) - \omega_0^2 M X_r = \omega_r M X_0 + \sum_{j=1}^{r-1} \omega_j M X_{r-j} - \sum_{j=1}^r (Q(U_j, X_{r-j}) + Q(X_{r-j}, U_j)). \quad (45)$$

Again, they all share the same linear operator  $L_t^0 - \omega_0^2 \mathbf{M}$  which must be decomposed only once for all  $\mathbf{X}_r$  ( $r = 0, 1, \dots, n$ ). The projection of Equations (44) and (45) onto the vibration mode  $\mathbf{X}_0$  gives:

- Order 1:

$$\omega_1 = \frac{\langle \mathbf{X}_0, \mathbf{Q}(\mathbf{U}_1, \mathbf{X}_0) \rangle + \langle \mathbf{X}_0, \mathbf{Q}(\mathbf{X}_0, \mathbf{U}_1) \rangle}{\langle \mathbf{M}\mathbf{X}_0, \mathbf{X}_0 \rangle} \quad (46)$$

- Order  $r$ :

$$\omega_r = \frac{\sum_{j=1}^r (\langle \mathbf{X}_0, \mathbf{Q}(\mathbf{U}_j, \mathbf{X}_{r-j}) \rangle + \langle \mathbf{X}_0, \mathbf{Q}(\mathbf{X}_{r-j}, \mathbf{U}_j) \rangle) - \sum_{j=1}^{r-1} \omega_j \langle \mathbf{X}_0, \mathbf{M}\mathbf{X}_{r-j} \rangle}{\langle \mathbf{M}\mathbf{X}_0, \mathbf{X}_0 \rangle} \quad (47)$$

The finite element discretization of the vibration problem gives:

- Order 1:

$$\begin{aligned} \omega_1 &= \frac{{}^t\{\mathbf{x}_0\}\{F_1\}}{{}^t\{\mathbf{x}_0\}[\mathbf{M}]\{\mathbf{x}_0\}} \\ ([\mathbf{K}_t^0] - \omega_0^2[\mathbf{M}])\{\mathbf{x}_1\} &= \omega_1[\mathbf{M}]\{\mathbf{X}_0\} + \{F_1\} \end{aligned} \quad (48)$$

- Order  $r$ :

$$\begin{aligned} \omega_r &= \frac{{}^t\{\mathbf{x}_0\}\{F_r\} - \sum_{j=1}^{r-1} \omega_j {}^t\{\mathbf{x}_0\}[\mathbf{M}]\{\mathbf{x}_{r-j}\}}{{}^t\{\mathbf{x}_0\}[\mathbf{M}]\{\mathbf{x}_0\}} \\ ([\mathbf{K}_t^0] - \omega_0^2[\mathbf{M}])\{\mathbf{x}_r\} &= \omega_r[\mathbf{M}]\{\mathbf{X}_0\} + \sum_{j=1}^{r-1} \omega_j[\mathbf{M}]\{\mathbf{x}_{r-j}\} + \{F_r\} \end{aligned} \quad (49)$$

where  $\{\mathbf{x}_r\}$  is the discretized form of  $\mathbf{u}_{x_r}$  and the vectors  $\{F_r\}$  depend only on the solutions up to order  $(r - 1)$ .

## 4 Numerical applications

In this section, a bifurcation analysis is conducted for a multilayer structure with nonlinear pre-buckling to evaluate the efficiency and robustness of bifurcation detection algorithms. We consider a cylindrical laminated roof composed of three orthotropic layers, see Figure 2. The thickness of each layer is the same. The top and bottom layers are oriented at  $45^\circ$  and the middle layer at  $0^\circ$  ( $45^\circ/0^\circ/45^\circ$ ). The material characteristics are given in Table 1. The roof is pinned on the two straight edges and free on the two others edges and subjected to point loading at its center. After a convergence study, the structure is discretized using 36 shell elements presented in Section 2.

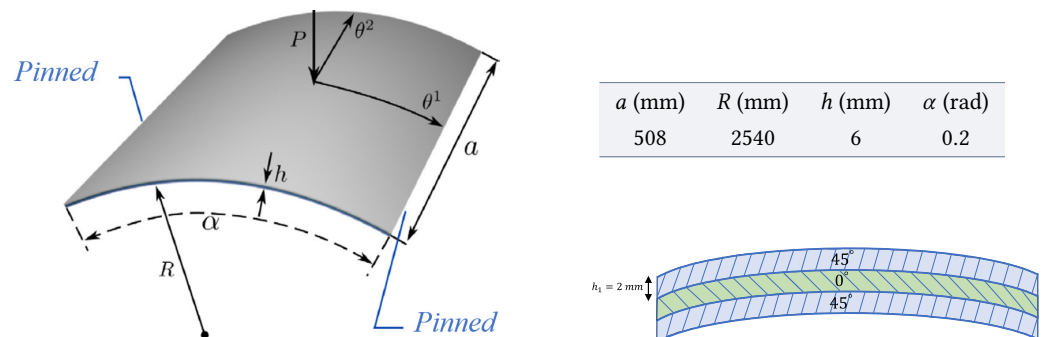


**Figure 2** Geometrical parameters of the cylindrical roof.

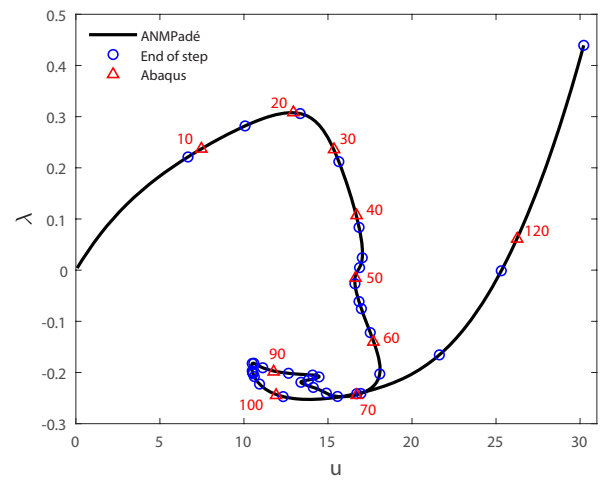
The response curve of the structure using the rational representation is given in Figure 3. Figure 4 shows the evolution of the structure's deformation along the equilibrium path of Figure 3. To reach a vertical displacement of the load application point of 30 mm, the ANM requires 35 steps (35 matrix decompositions) for truncation order  $n = 15$  and accuracy parameter  $\delta = 10^{-6}$

**Table 1** Mechanical properties of each roof layer.

	$E$ (MPa)	$\mu$		$G$ (MPa)	
$E_1$	3300	$\mu_{12}$	0.25	$G_{12}$	660
$E_2$	1100	$\mu_{23}$	0.25	$G_{23}$	440
$E_3$	1100	$\mu_{13}$	0.25	$G_{13}$	660

(the maximum residual of the solution path is equal to  $\log_{10}(\text{Res}) = -2.32$ ). A summary of the number of steps to have ( $u \approx 30$  mm) according to  $n$  and  $\delta$  is given in Table 2. The same problem is simulated using Abaqus with Newton Raphson algorithm and Riks control. The mesh is the same as the one used for the ANM with an eight node shell element S8R available in Abaqus/Standard. A displacement of 30 mm from the load application point requires 124 steps with 374 matrix decompositions using a fixed increment equal to 0.05 (or 62 steps with 203 matrix decompositions by using 0.1). This comparison shows the efficiency of the ANM.

**Figure 3** Load-vertical displacement of the load application point ( $n = 15$  and  $\delta = 10^{-6}$ ). Black line represents the response given by ANM with Padé approximation, circles are relative to the end of each ANM-Padé step and triangles represent 10 points of Abaqus-Riks response. Total number of steps: 124.



Depending on the parameters  $n$  and  $\delta$  and the technique used to represent the solution (polynomial or rational), the asymptotic numerical method allows us to observe different

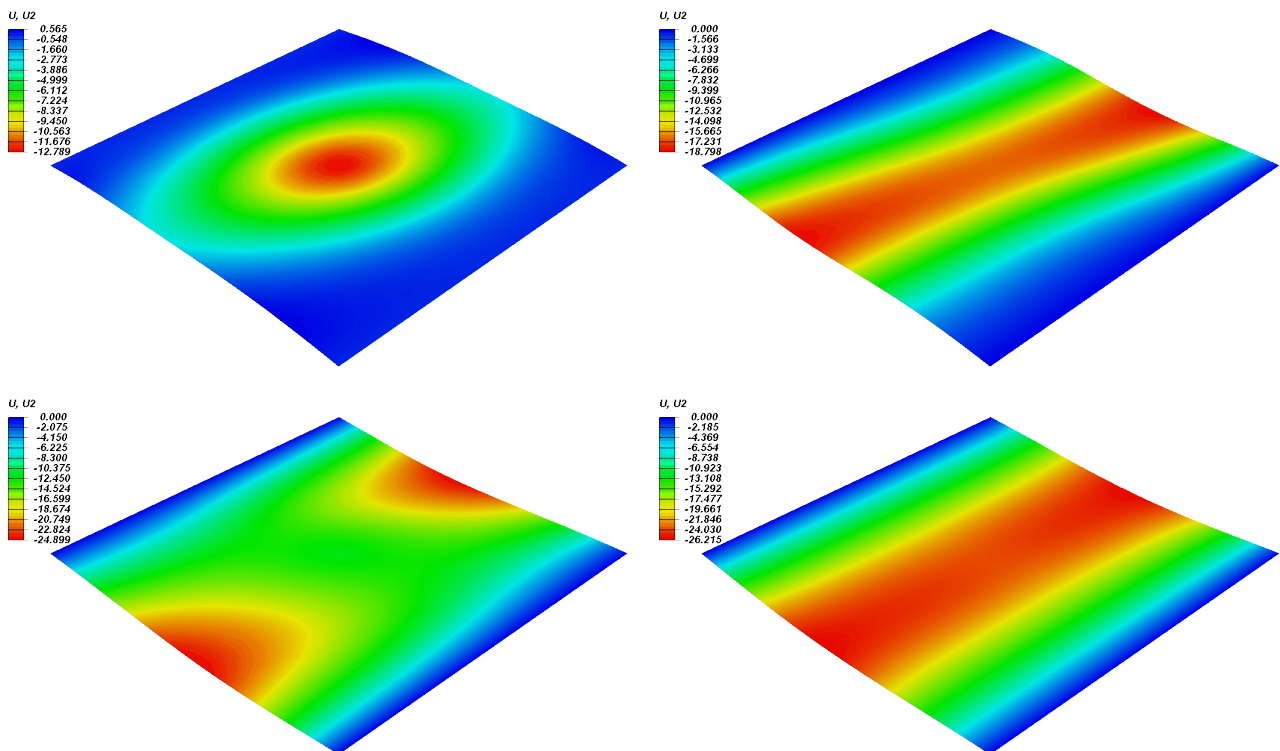


**Figure 4** Deformations of the structure at steps (a) 20, (b) 50, (c) 90, and (d) 120 in Figure 3.

**Table 2** Summary of the number of ANM-Padé steps to obtain a vertical displacement of the load application point of 30 mm as a function of the truncation order  $n$  and the accuracy  $\delta$ . The symbol (-) indicates that the corresponding parameters  $n$  and  $\delta$  do not give the same equilibrium path described in Figure 3.

$n \backslash \delta$	$10^{-6}$	$10^{-8}$	$10^{-10}$	$10^{-12}$
15	35	47	–	–
20	–	36	52	–
25	–	–	44	–
30	–	–	32	48

equilibrium paths, as shown in Figure 5. For  $n = 15$  and  $\delta = 10^{-6}$  with a polynomial representation, we notice a deviation of the curve at point C, followed by another deviation at point B, both of which are bifurcation points. The curve continues to follow the same path between C and B. Keeping the same representation, another equilibrium path is observed with  $n = 20$  and  $\delta = 10^{-8}$ . Points A and F are also bifurcation points for the structure. Two other bifurcation points (points D and E) appear with a rational representation with parameters  $n = 15$  and  $\delta = 10^{-10}$ . Therefore, a total of six bifurcation points can be identified using the three techniques described in Section 3. It should be noted that when the structure reaches these bifurcation points, it becomes unstable and significant changes in its shape may occur.

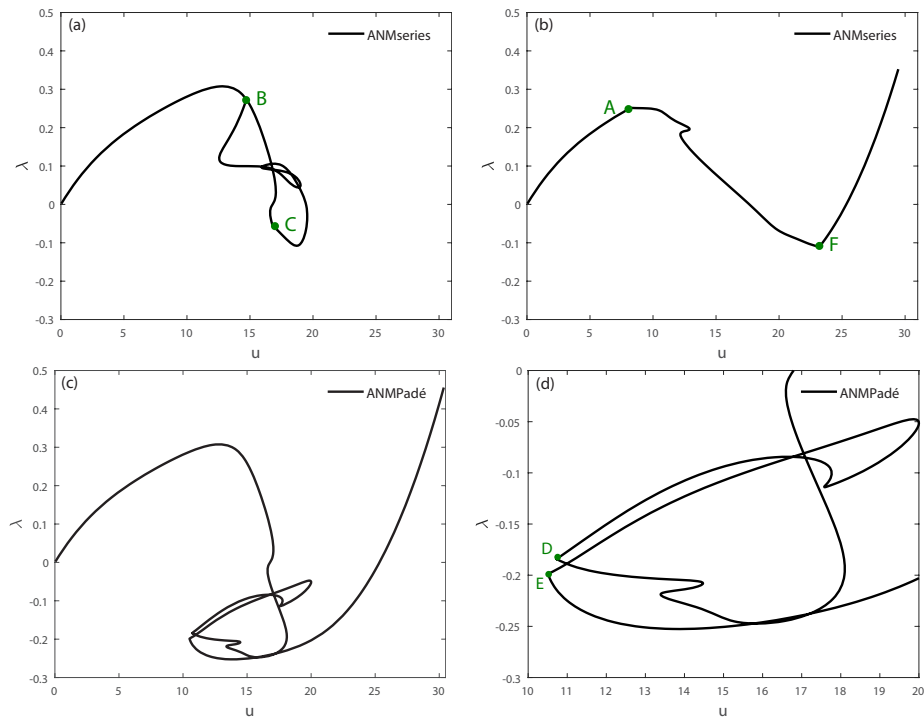


**Figure 5** Equilibrium paths of the structure as a function of representation type, truncation order  $n$  and accuracy parameter  $\delta$ : (a)  $n = 15$ ,  $\delta = 10^{-6}$ , series representation; (b)  $n = 20$ ,  $\delta = 10^{-8}$ , series representation; (c)  $n = 15$ ,  $\delta = 10^{-10}$ , Padé representation; (d) zoom of Figure 5(c) ( $u \in [10; 20]$  and  $\lambda \in [-0.3; 0]$ ).

The bifurcation indicator detects the six bifurcation points (Figure 6). It becomes zero exactly at the critical points. Table 3 shows the critical loading, detection step and residual at the end of the step for each bifurcation point, respectively. The residual remains quite small along the

Bifurcation point	A	B	C	D	E	F
critical loading $\lambda_c$	0.252	0.273	-0.054	-0.184	-0.199	-0.111
Step	2	4	9	23	26	34
$\log_{10}(\text{Res})$	-4.683	-4.448	-3.923	-4.383	-4.421	-2.319

**Table 3** Critical loading, detection step, and relative residual  $\text{Res} = \|F_{\text{int}} - F_{\text{ext}}\| / \|F_{\text{ext}}\|$  at each bifurcation point.

equilibrium branch.

The second technique for the detection bifurcation points is the pole analysis of the Padé approximants. Table 4 presents the real roots of the denominator of the Padé fractions in the

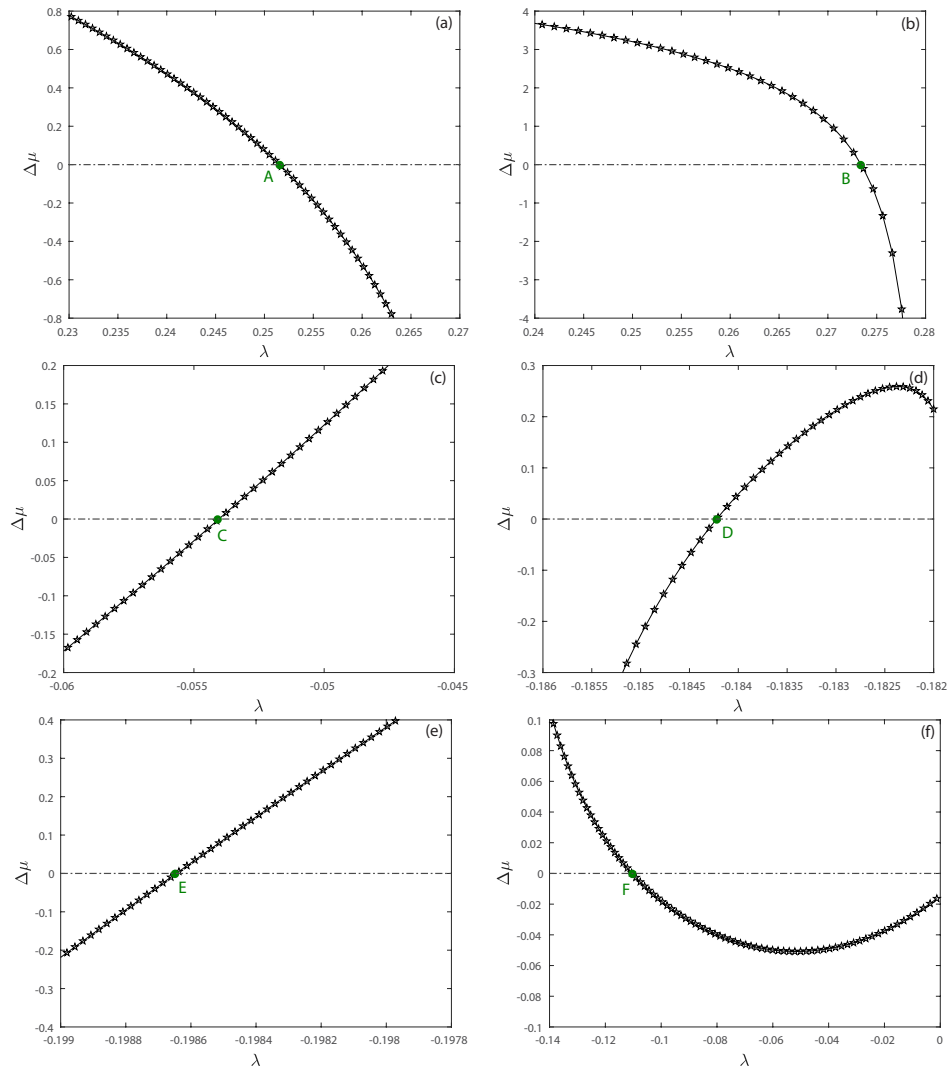


**Figure 6** Bifurcation indicator, along the equilibrium branch, as a function of the loading parameter for  $n = 15$  and  $\delta = 10^{-6}$  (Padé). Points A, B, C, D, E and F are the six bifurcation points of the structure.

vicinity of the bifurcation points for different truncation order  $n$  and accuracy parameter  $\delta$ . The poles shown are those belonging to the loading interval, and the three configurations analyzed give the same response as shown in Figure 3. We notice that the bifurcation points detected by the bifurcation indicator are among the poles. Taking the example of  $n = 15$  and  $\delta = 10^{-6}$ , the second step gives us a single pole ( $p_2 = 0.252$ ) that belongs to the loading interval and coincides exactly with the critical loading relative to the bifurcation point A. The same analysis for the fourth step leads to point B. Nevertheless, in step 9, we find two poles ( $p_{91} = -0.032$ ) and ( $p_{92} = -0.054 = \lambda_c(C)$ ). This can be attributed to defects in the rational representation because the pole  $p_{91}$  no longer appears by changing  $n$  and  $\delta$ . The same observation appears in the other situations where we find more than one pole. Thus, Padé approximants offer a useful tool for identifying bifurcation points without incurring any additional computational costs. To obtain reliable results, it is recommended to explore multiple configurations.

The third bifurcation analysis technique consists of tracking natural frequencies along the equilibrium path. Figure 7 shows the evolution of the relative frequency  $\beta$  for the first vibration mode as a function of the loading parameter  $\lambda$ . As with the bifurcation indicator,  $\beta$  is zero at the critical points and accurately detects the six bifurcation points.

In multilayer structures, the bifurcation points depend on the number of layers, orientation, thickness and mechanical properties of each layer. Thus, we tested two other roof configurations by changing the thickness ( $h = 9$  mm) and then the orientation of the layers while keeping the other parameters constant. Figure 8 shows the response curves for the two configurations as well as the bifurcation points, obtained using the techniques discussed previously, with the

Step	2	4	9	23	26	34
Loading	[0.221; 0.282]	[0.212; 0.306]	[-0.061; -0.026]	[-0.191; -0.182]	[-0.199; -0.197]	[-0.165; -0.001]
$\lambda_c$	0.252	0.273	-0.032	-0.184	-0.199	-0.111
			-0.054			
Step	2	5	13	30	39	49
Loading	[0.185; 0.274]	[0.263; 0.299]	[-0.055; -0.049]	[-0.186; -0.184]	[-0.199; -0.182]	[-0.197; -0.077]
$\lambda_c$	0.252	0.273	-0.054	-0.184	-0.184	-0.111
				-0.199	-0.130	
Step	2	6	18	33	37	46
Loading	[0.206; 0.265]	[0.273; 0.278]	[-0.056; -0.047]	[-0.189; -0.183]	[-0.199; -0.193]	[-0.203; -0.049]
$\lambda_c$	0.252	0.273	-0.054	-0.184	-0.199	-0.111
		0.274			-0.198	

**Table 4** Poles of the Padé approximants for three pairs of  $(n, \delta)$  in the vicinity of the bifurcation points. [top] ( $n = 15, \delta = 10^{-6}$ ), [middle] ( $n = 20, \delta = 10^{-10}$ ), [bottom] ( $n = 30, \delta = 10^{-12}$ ).

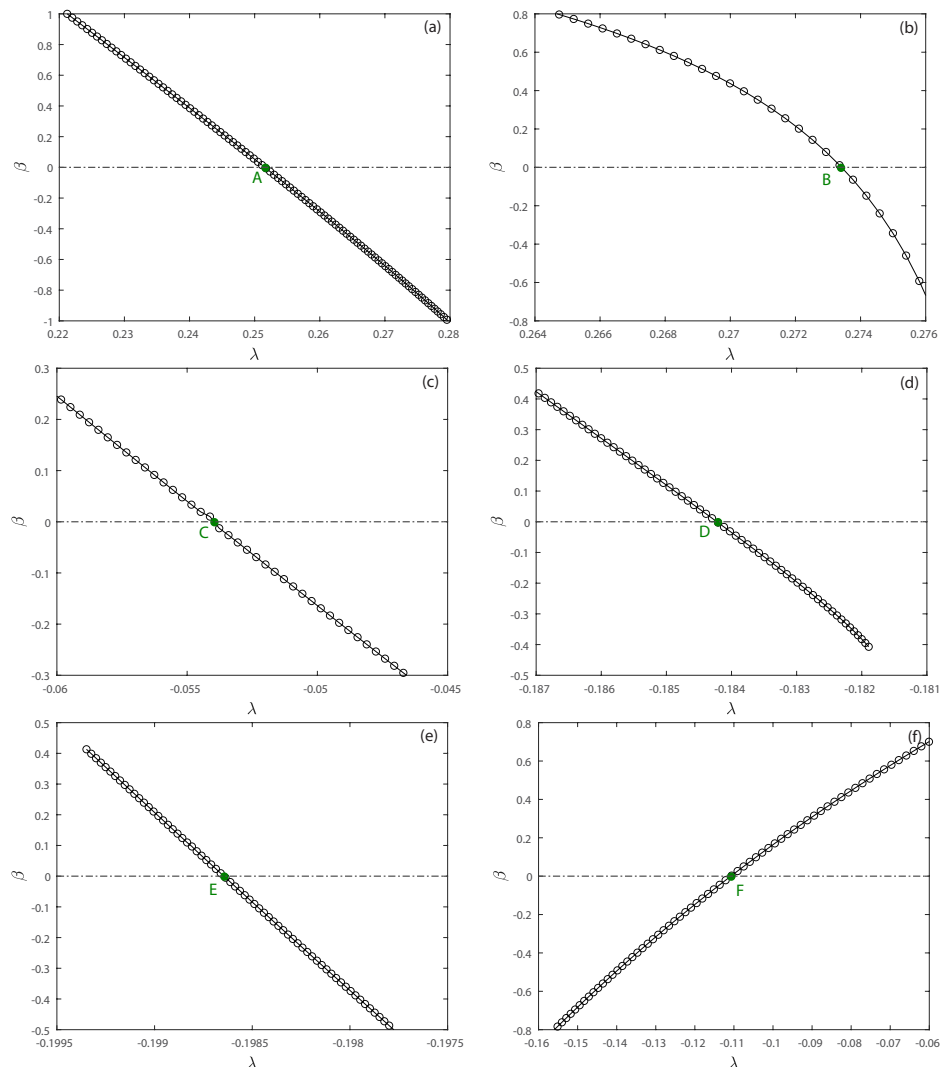


**Figure 7** Relative natural frequency  $\beta = \omega^2/\omega_0^2$ , along the equilibrium branch of Figure 3, as a function of the loading  $\lambda$  for the first vibration mode ( $n = 15$  and  $\delta = 10^{-6}$  with Padé representation). Points A, B, C, D, E and F are the six bifurcation points of the structure.

corresponding critical loads. These tests confirm the effectiveness of our algorithms for following equilibrium paths and detecting bifurcations.

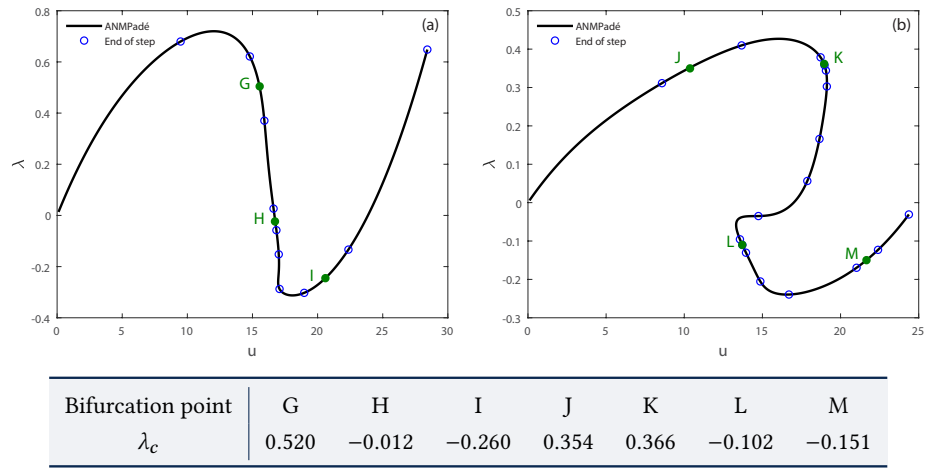


**Figure 8** Response curve for two different roof configurations by changing (a) the thickness ( $h = 9$  mm) and (b) the orientation of the layers ( $0^\circ/90^\circ/0^\circ$ ). The green points represent the bifurcation points and the corresponding table shows the critical loads.

## 5 Conclusion

In this work, we have presented a bifurcation analysis for multilayer structures using the asymptotic numerical method. Three bifurcation detection techniques have been discussed, enabling a comprehensive study of the instability of thin shell structures. The first technique is based on the bifurcation indicator, computed along the equilibrium branch, which vanishes exactly at critical points. By using a rational representation (Padé approximants) instead of a polynomial representation (Taylor series), the validity range of the solution is improved and bifurcations are detected by analyzing the roots of the denominators. The third technique combines buckling and vibration, where natural vibration frequencies detect bifurcations. According to the numerical tests conducted, all three techniques are highly accurate in detecting critical points, whatever the truncation order ( $15 \leq n \leq 30$ ) and the parameter ( $10^{-12} \leq \delta \leq 10^{-6}$ ). The ANM proves to be a highly efficient algorithm for studying instabilities and detecting bifurcation points in nonlinear prebuckling branches.

## A Finite element discretization

The fields  $\boldsymbol{v}$  and  $\boldsymbol{w}$ , which represent respectively the displacement and director difference, are interpolated via the shape functions of the classical eight node quadrilateral. By collecting the nodal values of  $\boldsymbol{v}$  and  $\boldsymbol{w}$  in the vector  $\{\boldsymbol{q}\}$ , the displacement  $\{\boldsymbol{u}\}$ , its virtual part  $\{\delta\boldsymbol{u}\}$  and its gradient  $\{\boldsymbol{\theta}(\boldsymbol{u})\}$  are related to nodal displacements  $\{\boldsymbol{q}\}$  and  $\{\delta\boldsymbol{q}\}$  through  $\{\boldsymbol{u}\} = [\boldsymbol{N}]\{\boldsymbol{q}\}$ ,  $\{\delta\boldsymbol{u}\} = [\boldsymbol{N}]\{\delta\boldsymbol{q}\}$  and  $\{\boldsymbol{\theta}(\boldsymbol{u})\} = [\boldsymbol{G}]\{\boldsymbol{q}\}$  where  $[\boldsymbol{N}]$  is the shape function matrix and  $[\boldsymbol{G}]$  is their gradient matrix.

The Green-Lagrange strain (compatible part) is expressed in the covariant basis as:

$$\boldsymbol{\gamma}_{ij}(\boldsymbol{u}) = \frac{1}{2} \left( \frac{\partial \boldsymbol{u}}{\partial \theta^i} \boldsymbol{g}_j + \frac{\partial \boldsymbol{u}}{\partial \theta^j} \boldsymbol{g}_i + \frac{\partial \boldsymbol{u}}{\partial \theta^i} \frac{\partial \boldsymbol{u}}{\partial \theta^j} \right) \quad (\text{A.1})$$

where  $\boldsymbol{g}_i$  represents the covariant basis vectors.  $\boldsymbol{\gamma}_u$  can be decomposed into a linear part  $\boldsymbol{\gamma}_l(\boldsymbol{u})$  and a nonlinear part  $\boldsymbol{\gamma}_{nl}(\boldsymbol{u}, \boldsymbol{u})$ , that is  $\boldsymbol{\gamma}_u = \boldsymbol{\gamma}_l(\boldsymbol{u}) + \boldsymbol{\gamma}_{nl}(\boldsymbol{u}, \boldsymbol{u})$  with

$$\boldsymbol{\gamma}_l = [\boldsymbol{R}]\{\boldsymbol{\theta}(\boldsymbol{q})\} = [\boldsymbol{R}][\boldsymbol{G}]\{\boldsymbol{q}\} \quad \text{and} \quad \boldsymbol{\gamma}_{nl} = \frac{1}{2}[\boldsymbol{A}(\boldsymbol{q})]\{\boldsymbol{\theta}(\boldsymbol{q})\} = \frac{1}{2}[\boldsymbol{A}(\boldsymbol{q})][\boldsymbol{G}]\{\boldsymbol{q}\}. \quad (\text{A.2})$$

The virtual strain then reads

$$\delta\boldsymbol{\gamma} = ([\boldsymbol{R}] + [\boldsymbol{A}(\boldsymbol{q})])[\boldsymbol{G}]\{\delta\boldsymbol{q}\} = [\bar{\boldsymbol{B}}]\{\delta\boldsymbol{q}\} \quad (\text{A.3})$$

with  $[\bar{\boldsymbol{B}}] = ([\boldsymbol{R}] + [\boldsymbol{A}(\boldsymbol{q})])[\boldsymbol{G}]$  where  $[\boldsymbol{R}]$  and  $[\boldsymbol{A}(\boldsymbol{q})]$  represent the component matrix of the covariant basis and the displacement gradient matrix, respectively.

For the enhanced assumed strain  $\tilde{\boldsymbol{\gamma}} = \theta_3 \tilde{\beta}_{33} \mathbf{g}^3 \otimes \mathbf{g}^3$ , the component  $\tilde{\beta}_{33}$  does not require any inter-element continuity. Thus, it is discretized as a bilinear polynomial  $\tilde{\beta}_{33} = \alpha_1 + \alpha_2 \xi + \alpha_3 \eta + \alpha_4 \xi \eta$  where  $\xi$  and  $\eta$  represent the isoparametric coordinates. The unknown parameters  $\alpha_1$ ,  $\alpha_2$ ,  $\alpha_3$  and  $\alpha_4$  can be eliminated at the elementary level (Büchter et al. 1994). Thus, the additional deformation is written in the matrix form

$$\{\tilde{\boldsymbol{\gamma}}\} = [\mathbf{B}_\alpha] \{\boldsymbol{\alpha}\}. \quad (\text{A.4})$$

By substituting Equations (A.2) to (A.4) into Equation (23), we obtain the discretized form which represents the equilibrium of structure:

$$\begin{aligned} [\mathbf{K}_t^0] \{\mathbf{q}_p\} &= \lambda_p \{\mathbf{F}\} + \{\mathbf{F}_p\} - [\mathbf{K}_{\alpha u}] [\mathbf{K}_{\alpha \alpha}]^{-1} \{\mathbf{R}_p^\alpha\} \\ [\mathbf{K}_{\alpha \alpha}] \{\boldsymbol{\alpha}_p\} + [\mathbf{K}_{\alpha u}] \{\mathbf{q}_p\} &= \{\mathbf{R}_p^\alpha\} \\ {}^t \{\mathbf{q}_p\} \{\mathbf{q}_1\} + \lambda_p \lambda_1 &= 0 \end{aligned} \quad (\text{A.5})$$

with

$$[\mathbf{K}_{\alpha \alpha}] = \sum_{m=1}^N \int_{\Omega} ({}^t [\mathbf{B}_\alpha] [\mathbf{D}]^m [\mathbf{B}_\alpha]) dv \quad (\text{A.6})$$

$$[\mathbf{K}_{\alpha u}] = \sum_{m=1}^N \int_{\Omega} ({}^t [\mathbf{B}_\alpha] [\mathbf{D}]^m [\bar{\mathbf{B}}]) dv \quad (\text{A.7})$$

$$[\mathbf{K}_{uu}] = \sum_{m=1}^N \int_{\Omega} ({}^t [\bar{\mathbf{B}}] [\mathbf{D}]^m [\bar{\mathbf{B}}] + {}^t [\mathbf{G}] [\mathbf{P}]^m [\mathbf{G}]) dv \quad (\text{A.8})$$

and  $[\mathbf{K}_t^0] = [\mathbf{K}_{uu}] - [\mathbf{K}_{\alpha u}] [\mathbf{K}_{\alpha \alpha}]^{-1} [\mathbf{K}_{\alpha u}]$  where  $[\mathbf{K}_t^0]$  is the tangent stiffness matrix,  $\{\mathbf{F}\}$  the external load vector and  $[\mathbf{P}]^m$  the initial stress matrix in  $m$ th layer. Compared to Riks method, the new terms are the right-hand nonlinear terms  $\{\mathbf{F}_p\}$  and  $\{\mathbf{R}_p^\alpha\}$  related to solutions at previous orders. These two terms are expressed as follows:

$$\{\mathbf{F}_p\} = - \sum_{m=1}^N \left\{ \int_{\Omega} \left( {}^t [\mathbf{G}] \sum_{r=1}^{p-1} {}^t [\mathbf{A}(\mathbf{q}_{p-r})] \{\mathbf{S}_r\}^m + {}^t [\bar{\mathbf{B}}(\mathbf{q}_0)] [\mathbf{D}]^m \sum_{r=1}^{p-1} \frac{1}{2} [\mathbf{A}(\mathbf{q}_{p-r})] \{\boldsymbol{\theta}(\mathbf{q}_r)\} \right) dv \right\} \quad (\text{A.9})$$

and

$$\{\mathbf{R}_p^\alpha\} = - \sum_{m=1}^N \left\{ \int_{\Omega} \left( {}^t [\mathbf{B}_\alpha] [\mathbf{D}]^m \sum_{r=1}^{p-1} \frac{1}{2} [\mathbf{A}(\mathbf{q}_{p-r})] \{\boldsymbol{\theta}(\mathbf{q}_r)\} \right) dv \right\} \quad (\text{A.10})$$


## References

- Abichou, H., H. Zahrouni, and M. Potier-Ferry (2002). Asymptotic numerical method for problems coupling several nonlinearities. *Computer Methods in Applied Mechanics and Engineering* 191(51-52):5795–5810. [DOI], [HAL].
- Assidi, M., H. Zahrouni, N. Damil, and M. Potier-Ferry (2009). Regularization and perturbation technique to solve plasticity problems. *International Journal of Material Forming* 2(1):1–14. [DOI], [HAL].
- Azrar, L., B. Cochelin, N. Damil, and M. Potier-Ferry (1993). An asymptotic-numerical method to compute the postbuckling behaviour of elastic plates and shells. *International Journal for Numerical Methods in Engineering* 36(8):1251–1277. [DOI], [HAL].
- Baker, G. A. and P. Graves-Morris (1981). Padé approximants. Part 1: Basic theory. *Encyclopedia of Mathematics and Its Applications*, 276–334. [DOI].
- Boutyour, E. H., H. Zahrouni, M. Potier-Ferry, and M. Boudi (2004). Bifurcation points and bifurcated branches by an asymptotic numerical method and Padé approximants. *International Journal for Numerical Methods in Engineering* 60(12):1987–2012. [DOI], [HAL].



- Boutyour, E., L. Azrar, and M. Potier-Ferry (2006). Vibration of buckled elastic structures with large rotations by an asymptotic numerical method. *Computers & Structures* 84(3-4):93–101. [DOI], [HAL].
- Brunetti, M., S. Vidoli, and A. Vincenti (2018). Bistability of orthotropic shells with clamped boundary conditions: an analysis by the polar method. *Composite Structures* 194:388–397. [DOI], [HAL].
- Büchter, N., E. Ramm, and D. Roehl (1994). Three-dimensional extension of non-linear shell formulation based on the enhanced assumed strain concept. *International Journal for Numerical Methods in Engineering* 37(15):2551–2568. [DOI].
- Cadou, J. M., M. Potier-Ferry, B. Cochelin, and N. Damil (2001). ANM for stationary Navier-Stokes equations and with Petrov-Galerkin formulation. *International Journal for Numerical Methods in Engineering* 50(4):825–845. [DOI], [HAL].
- Cochelin, B. (1994). A path-following technique via an asymptotic-numerical method. *Computers & Structures* 53(5):1181–1192. [DOI], [HAL].
- Cochelin, B., N. Damil, and M. Potier-Ferry (1994). The asymptotic-numerical method: an efficient perturbation technique for nonlinear structural mechanics. *Revue Européenne des Éléments Finis* 3(2):281–297. [DOI], [HAL].
- Cochelin, B., N. Damil, and M. Potier-Ferry (2007). *Méthode asymptotique numérique*. Hermès-Lavoissier. ISBN: 9782746215672.
- Damil, N. and M. Potier-Ferry (1990). A new method to compute perturbed bifurcations: application to the buckling of imperfect elastic structures. *International Journal of Engineering Science* 28(9):943–957. [DOI], [HAL].
- Diaconu, C. G., P. M. Weaver, and F. Mattioni (2008). Concepts for morphing airfoil sections using bi-stable laminated composite structures. *Thin-Walled Structures* 46(6):689–701. [DOI].
- El Chebair, A., M. Païoussis, and A. Misra (1989). Experimental study of annular-flow-induced instabilities of cylindrical shells. *Journal of Fluids and Structures* 3(4):349–364. [DOI].
- Elhage-Hussein, A., M. Potier-Ferry, and N. Damil (2000). A numerical continuation method based on Padé approximants. *International Journal of Solids and Structures* 37(46-47):6981–7001. [DOI], [HAL].
- Finot, M. and S. Suresh (1996). Small and large deformation of thick and thin-film multi-layers: effects of layer geometry, plasticity and compositional gradients. *Journal of the Mechanics and Physics of Solids* 44(5):683–721. [DOI].
- Frulloni, E., J. Kenny, P. Conti, and L. Torre (2007). Experimental study and finite element analysis of the elastic instability of composite lattice structures for aeronautic applications. *Composite Structures* 78(4):519–528. [DOI].
- Fu, T., X. Wu, Z. Xiao, and Z. Chen (2021). Dynamic instability analysis of FG-CNTRC laminated conical shells surrounded by elastic foundations within FSDT. *European Journal of Mechanics - A/Solids* 85:104139. [DOI].
- Kim, D.-H., S.-J. Joo, D.-O. Kwak, and H.-S. Kim (2015). Anisotropic viscoelastic shell modeling technique of copper patterns/photoimageable solder resist composite for warpage simulation of multi-layer printed circuit boards. *Journal of Micromechanics and Microengineering* 25(10):105016. [DOI].
- Kuang, Z., Q. Huang, W. Huang, J. Yang, H. Zahrouni, M. Potier-Ferry, and H. Hu (2021). A computational framework for multi-stability analysis of laminated shells. *Journal of the Mechanics and Physics of Solids* 149:104317. [DOI], [HAL].
- Kumar Yadav, K. and S. Gerasimidis (2019). Instability of thin steel cylindrical shells under bending. *Thin-Walled Structures* 137:151–166. [DOI].
- Najah, A., B. Cochelin, N. Damil, and M. Potier-Ferry (1998). A critical review of asymptotic numerical methods. *Archives of Computational Methods in Engineering* 5(1):31–50. [DOI], [HAL].
- Noor, A. K. and J. M. Peters (1980). Reduced basis technique for nonlinear analysis of structures. *AIAA Journal* 18(4):455–462. [DOI].
- Ramm, E. (2012). *Buckling of Shells. Proceedings of a State-of-the-Art Colloquium, Universität Stuttgart, Germany, May 6-7, 1982*. Springer Berlin Heidelberg. [DOI].
- Simo, J. C. and M. S. Rifai (1990). A class of mixed assumed strain methods and the method of

- incompatible modes. *International Journal for Numerical Methods in Engineering* 29(8):1595–1638. [DOI].
- Toor, Z. S. (2018). Space applications of composite materials. *Journal of Space Technology* 8(1):65–70. [OA].
- Tri, A., H. Zahrouni, and M. Potier-Ferry (2014). Bifurcation indicator based on meshless and asymptotic numerical methods for nonlinear Poisson problems. *Numerical Methods for Partial Differential Equations* 30(3):978–993. [DOI], [OA].
- Wang, Y., K. Low, H. Pang, K. Hoon, F. Che, and Y. Yong (2006). Modeling and simulation for a drop-impact analysis of multi-layered printed circuit boards. *Microelectronics Reliability* 46(2-4):558–573. [DOI].
- Wang, Z., C. Luan, G. Liao, J. Liu, X. Yao, and J. Fu (2020). Progress in auxetic mechanical metamaterials: structures, characteristics, manufacturing methods, and applications. *Advanced Engineering Materials* 22(10):2000312. [DOI].
- Xu, R., Y. Hui, H. Hu, Q. Huang, H. Zahrouni, T. Ben Zineb, and M. Potier-Ferry (2019). A Fourier-related  $FE^2$  multiscale model for instability phenomena of long fiber reinforced materials. *Composite Structures* 211:530–539. [DOI], [HAL].
- Zahrouni, H., B. Cochelin, and M. Potier-Ferry (1999). Computing finite rotations of shells by an asymptotic numerical method. *Computer Methods in Applied Mechanics and Engineering* 175(1-2):71–85. [DOI], [HAL].
- Zhao, G. and T. Fu (2023). A unit compound structure design: Poisson's ratio is autonomously adjustable from negative to positive. *Materials* 16(5):1808. [DOI], [OA].
- Zhao, G., T. Fu, and J. Li (2023). Study on Concave Direction Impact Performance of Similar Concave Hexagon Honeycomb Structure. *Materials* 16(8):3262. [DOI], [OA].
- Zhou, X., L. Ren, Z. Song, G. Li, J. Zhang, B. Li, Q. Wu, W. Li, L. Ren, and Q. Liu (2023). Advances in 3D/4D printing of mechanical metamaterials: From manufacturing to applications. *Composites Part B: Engineering* 254:110585. [DOI].

**Open Access** This article is licensed under a Creative Commons Attribution 4.0 International License, which permits use, sharing, adaptation, distribution and reproduction in any medium or format, as long as you give appropriate credit to the original author(s) and the source, provide a link to the Creative Commons license, and indicate if changes were made. The images or other third party material in this article are included in the article's Creative Commons license, unless indicated otherwise in a credit line to the material. If material is not included in the article's Creative Commons license and your intended use is not permitted by statutory regulation or exceeds the permitted use, you will need to obtain permission directly from the authors—the copyright holder. To view a copy of this license, visit [creativecommons.org/licenses/by/4.0](https://creativecommons.org/licenses/by/4.0). 

**Authors' contributions** HA: Writing-original draft, Conceptualization, Software, Validation, Investigation, Review and Editing. HZ and NM: Supervision, Project administration, Conceptualization, Review and Editing. PV and MB: Software, Validation, Investigation, Review and Editing. MPF: Project administration, Conceptualization, Review and Editing.

**Supplementary Material** Some of the results exposed in the present paper can be reproduced using the datasets archived at the permalink [10.5281/zenodo.14764156](https://zenodo.org/record/14764156). The folder also contains the figures in raw format.

**Competing interests** The authors declare that they have no competing interests.

**Journal's Note** JTCAM remains neutral with regard to the content of the publication and institutional affiliations.